

FABRICATION AND CHARACTERIZATION OF MULTILAYER mSiO₂@Fe₃O₄@Au MESOPOROUS NANOCOMPOSITE FOR NEAR- INFRARED BIOMEDICAL APPLICATIONS

Mohammad Khosroshahi ^{a,b,*}, Iman Manavi Tehrani ^c, Alireza Nouri ^d

^a Laser and Nanobiophotonics Laboratory, Biomaterial Group, Faculty of Biomedical Engineering, Amirkabir University of Technology, Tehran, Iran

^b MIS-Electronics, Nanobiophotonics and Biomedical Research Lab, Richmond Hill, ON, Canada

^c The University of Sydney, School of Chemical and Biomolecular Engineering, Sydney, 2006, Australia

^d Smarter Alloys Inc., 75 Bathurst Drive, Suite B, Waterloo, Ontario N2V 1N2, Canada
(khosrom@mie.utoronto.ca)

Article History:

Received 06 January 2018
Revised 21 February 2018
Accepted 24 February 2018

Keywords:

Mesoporous
nanocomposite
Silica
Magnetite
Gold coating
Near IR
Photothermal applications

Abstract:

Gold coated mesoporous silica magnetic nanocomposite (mSiO₂@Fe₃O₄@Au) was synthesized using ethylene glycol (EG) as template at two different ratios of EG: TEOS of 0.1 and 0.6. The chemistry, morphology, optical and magnetic properties of the obtained nanocomposites were characterized by Fourier Transform (FTIR), Scanning Electron Microscopy (SEM), Transverse Electron Microscopy (TEM), Atomic Force Microscopy (AFM), X-ray Diffractometry (XRD), Vibrating Sample Magnetometry (VSM) and UV-Vis absorption spectroscopy. The mean diameter of amino-functionalized SiO₂ NPs was measured 70 nm. The range of porosity ranged from 10 to 100 nm, with larger distribution of pore size of less than 20 nm. The average radius of pores on SiO₂ NPs calculated by BJH method is approximately 15.5 nm. Magnetic nanoparticles (MNPs) with the average diameter of 34 nm were synthesized and then coated by AuNPs with an average size of 25 nm synthesized via a two-step process of dative and reduction method. The average size distribution of mSiO₂@Fe₃O₄@Au nanocomposite was measured about 157 nm. The nanocomposite exhibited a significant red-shift in surface plasmon resonance wavelength ($\lambda_{SPR} \approx 800$ nm), which coincides with NIR biomedical applications.

1. Introduction

Despite the novel and strongly dependent properties of nanoparticles (NPs) on size, shape and surface configuration which make them different to their counterpart bulk materials, there has recently been a great interest in the development of nanoparticles that combine multiple functions or properties that are not easily obtainable by an individual material. Over the past decades, the development of inorganic nanoparticles such as

magnetic NPs (MNPs) especially magnetite (Fe₃O₄), gold nanoparticles (AuNPs), and availability of multi-nanostructures with highly controlled magnetic and opto-thermal has created wide-spread interest in the use of these NPs in biological systems for diagnostic, bioimaging, drug delivery and therapeutic applications due to their biocompatibility because of their inert surface, nontoxicity and surface conjugation chemistry, i.e., they can be linked to specific ligands for tumor targeting [1-6]. However,

magnetic nanoparticles are prone to aggregation due to anisotropic dipolar attraction and rapid biodegradation when they are exposed to biological systems [7]. For this reason, the doping of magnetic nanoparticles into a silica matrix can successfully prevent magnetic nanoparticles from self-aggregation and from reacting with environmental species [8]. Moreover, the magnetic/silica nanocomposites (with the magnetic core (Fe_3O_4) and mesoporous silica shell) shows ease of functionalization as well as resistance to chemicals and high temperatures [9]. By absorbing a suitable wavelength from laser beams, the acquired energy is transferred to heat through the photothermal mechanism which results in an irreversible damage to the target cells.

Among the inorganic materials, mesoporous silica ($m\text{SiO}_2$) have also attracted attention since its first discovery in the early 1990s due to their high surface areas, well-defined pore structures, and tunable pore sizes because silica is nontoxic and highly biocompatible material [10-12]. A significant progress since then has been achieved in multifunctional nanocarriers due to formation of mesostructures attributed to the cooperative assembly of structural agents such as surfactant molecules, and silica precursors through the sol-gel process [13]. Once, the template is removed, the mesostructures of MSNs will provide distinct regions of silica framework, pores and outer surface. It can be synthesized simultaneously or by coating a thin silica layer on magnetic nanoparticles [7,14]. Another way is to incorporate magnetic nanoparticles into a silica matrix or to embed the synthesized nanomagnetic particles into the mesopores via physical or chemical bonding [15]. Lu et al. [16] reported a new method for fabricating magnetic mesoporous silica with open pores by grafting cobalt nanoparticles on the outer surface of the SBA-15 particles. Wu et al. [14] synthesized magnetic composite with mesoporous silica being coated on Fe_3O_4 cores. However, the shape of the resultant magnetic particles is irregular with a wide particle size distribution from hundreds of nanometers to several microns.

The major advantages of such as system for biomedical applications include: (a) imaging using fluorescent agents, (b) drug delivery due to various mesopores and using magnetic nanoparticles. High surface area ($> 900 \text{ m}^2\text{g}^{-1}$) and large pore volume ($>$

$0.9 \text{ cm}^3\text{g}^{-1}$) of MSNs provides a sufficient space to host or encapsulate relatively large amounts of bioactive molecules and therapeutic drugs [17, 18]. The size of mesopores can be tailored in order to entrap little molecules or large nanoparticles via chemical bonding or physical adsorption. MSNs can deliver drugs and therapeutic biomolecules owing to their high loading efficiency within the pores [19,20]. With the use of various dopants, regular fluorophores, drug molecules, quantum dots, etc. new properties can be added to the host silica matrix [21], and (c) targeted delivery because the outer surface with many silanol groups can be modified with specific ligands [13]. The presence of silanol groups in both interior and exterior surfaces of MSNs make it easy to combine with various nanoparticles through covalent and/or electrostatic self-assembly [22].

An ideal photo-absorbing agent should have strong light absorbance in the near-infrared (NIR) tissue transparency window (750-1300 nm) [23]. MSNs are effectively transparent in the sense that they absorb light in the NIR, visible, and ultraviolet (UV) regions. This enables MSNs to exhibit a combined optical and magnetic properties in the presence of magnetic materials. Combination of $m\text{SiO}_2$ with MNPs produces a hybrid system that can be utilized through the use of a magnetic field. Lu et al. [24] prepared magnetic iron oxide-loaded hollow mesoporous silica nanocapsules with a particle size of 100 nm, and they found that magnetic nanocapsules induced heating upon exposure to magnetic field and remotely triggered drug release. Recently, Shao et al. [25] reported the shape effect of magnetic MSNs on endocytosis and biocompatibility. While long-rod magnetic MSNs showed higher intracellular internalization amount than their short-rod and the sphere-like counterparts in both cancer cells and normal cells, there was no significant shape effects on biocompatibility. However, the use of bulk MSNs alone in many applications, particularly in targeted drug delivery mechanisms as carrier suffers from few inherent limitations [26]. Now, when magnetic/silica nanocomposites are coated with a suitable gold shell thickness, the treatment efficiency will be enhanced in the NIR region is largely increased [27-29]. This is due to AuNPs unique optical properties such as strong localized surface plasmon resonance (LSPR), surface-enhanced scattering, non-linear optical properties, tunable

resonance across the Vis-NIR due to adjustable nanoparticle size and shape as well others factors mentioned above [7-9, 30].

Recently, we have described the results of laser wavelengths and gold nanoshells on drug release and magnetic guidance on uptake by cancer cells [31], doxorubicin loaded magnetoplasmonic thermosensitive liposomes which were designed to combine features of magnetic drug targeting and laser hyperthermia-triggered drug release for breast cancer [6] and the magnetodendrimer samples conjugated by folic acid molecules for targeting and by gold nanoparticles for photothermal hyperthermia purpose [32]. Following the above arguments and our results, here we report the results of preparation and characterization of ($m\text{SiO}_2@Fe_3O_4 @Au$) using the template technique at two different concentrations of Ethylene glycol. (EG).

1. Materials and Methods

1.1. Materials

Tetraethyl orthosilicate (TEOS; $C_8H_{20}O_4Si$; Merck), Ethanol (C_2H_5OH , Merck), Ammonium hydroxide (NH_4OH), (3-aminopropyl) triethoxysilane (APTES), Sodium hydroxide (NaOH, Merck, 97%), Iron(III) Chloride hexahydrate ($FeCl_3 \cdot 6H_2O$, 99%), Iron(II) chloride tetrahydrate ($FeCl_2 \cdot 4H_2O$, 99%), Hydrochloric acid (HCl, 37%), Sodium citrate tribasic dihydrate ($C_6H_5Na_3O_7 \cdot 2H_2O$), Ethylene glycol monomers ($C_2H_6O_2$, Iran), Trisodium citrate ($Na_3C_6H_5O_7$), tetraethylorthosilicate (TEOS- $C_8H_{20}O_4Si$), Chloroauric acid ($HAuCl_4$, Aldrich 99.9 %). Reagents were all used as received.

1.2. Characterization

The chemical structure of the synthesized nanoparticles was characterized by Fourier-transform infrared spectroscopy (FTIR-8300, Shimadzu, Japan). The crystal structure of nanoparticles was determined by X-ray diffraction (XRD- FK60-40) using Cu $K\alpha$ radiation at $\lambda = 0.15406$ nm, Particle size distribution was measured using a Malvern Instruments Mastersizer 2000 with a Hydro 2000S side feeder. The morphology of silica nanoparticles as well as the structure of MSNs were characterized by scanning electron microscopy (SEM; stereoscan S360 Cambridge) and energy-dispersive X-ray spectrometry (EDAX). The UV absorption spectra of

gold nanoparticles and gold-coated magnetic/mesoporous silica nanocomposites were recorded by Shimadzu UV-3101PC UV-Vis absorption spectrophotometer. 77 K nitrogen adsorption/desorption technique was used for determining surface area and pore size distribution in MSNs. Brunauer–Emmett–Teller (BET) and Barrett–Joyner–Halenda (BJH) models are commonly used analytic methods for adsorption/desorption isotherm. This was done on BJH plotting by Quanta chrome TPR Win v1.0 using nitrogen as the sorbate. Magnetization measurements were carried out at 300 K in a magnetic field (H) of up to 20 KOe with a vibrating sample magnetometer (VSM-PAR155) that can measure magnetic moments as low as 10^{-3} emu.

1.3. Synthesis of NH_2 functionalized silica (SiO_2) nanoparticles

Stober method was applied to fabricate silica nanoparticles. A solution consisting of 40 mL of water and 160 mL of ethanol with the volume ratio of 1 to 4 was prepared. 1 mL of ammonia was added into the solution under continued stirring and was stirred for 15 min. Then, 4 mL of TEOS was added drop-wise for 30 min to the above solution. The clear solution gradually turned into milky colour and was left under vigorous stirring for 24 h. After that, a reflux column was set up at 80 °C. During the reflux process, which took 1 h, 25 μL of APTES was added in order to functionalize the surface of the nanoparticles with NH_2 groups. The resultant solution was centrifuged three times and each time the solution was washed with ethanol in order to remove the supernatant. The solution was freeze-dried at -60 °C and white uniform silica nanoparticles were obtained. The functionalization reaction could be verified by stopping the stir-ring and observing the separation of the mixture to two layers: the APTES-coated nanosilica particles precipitated at the bottom of the reactor and a clear solution remained at the top.

1.4. Synthesis of mesoporous silica nanoparticles ($mSiO_2$)

Mesoporous silicas of the MSU-X type were made with sodium citrate tribasic dihydrate surfactant and (EG) monomers as template to form pores in the silica structure during the synthesis. Sodium hydroxide was used for controlling the pH. Ethylene glycols were decomposed with increasing the temperature, leaving

the occupied spaces to become pores. The degree of porosity is dependent on the concentration of EG. In the present study, two samples of MSNs with 30% and 60% porosities were fabricated. First, in two different containers similar solutions of 40 mL water and 160 mL ethanol with the volume ratio of 1 to 4 were prepared and then 1 mL of ammonia was added into each solution under continued stirring. For the synthesis of MSNs, the ratio of TEOS to EG were 0.1 and 0.6 for 30% and 60% porosity respectively. TEOS was added drop-wise to the solution after the addition of EG. Both solutions were under vigorous stirring for 24 h. After setting up a reflux system, the solution was heated at 80 °C and stirred for 1 h. At this stage, APTES was added to immobilize amino groups on the surface. After three times centrifugation at 4000 rpm for 15 min, the resulting powder was dried in the oven for 12 h under 50 °C in order to obtain a white powder. For calcinations and fully decomposition of EG, the obtained powder was further heated in the oven for 6 h at 560 °C to evaporation of EG monomers. It is notable that MSNs can be obtained after removing the surfactant template by calcination or dissolution with an appropriate solvent [2]. Finally, due to the presence of carbon group in the structure, a black powder was obtained.

1.5. Synthesis of Fe_3O_4

Stock solutions of 1.28 M Iron (III) ferric chloride hexahydrate ($FeCl_3 \cdot 6H_2O$), 0.64 M Iron (II) ferrous chloride tetrahydrate ($FeCl_2 \cdot 4H_2O$) and 0.4 M HCl were prepared as a source of iron by dissolving the respective chemicals in milli-Q water (18.2 M) under vigorous stirring. The solution was deoxygenated by passing N_2 gas for 1h prior to the use). In the same way, stock solutions of 0.9 M NaOH were prepared as the alkali sources. Aqueous dispersion of magnetic nanoparticles was prepared by alkalizing an aqueous mixture of ferric and ferrous salts with NaOH at room temperature. 25 mL of this solution was added drop-wise into iron salt source under vigorous magnetic stirring at 1000 rpm for 30 min at ambient temperature. A complete precipitation of Fe_3O_4 should be expected between 7.5–14 pH, which in our case was 10, while maintaining a molar ratio of $Fe^{2+}:Fe^{3+} = 1:2$ under a non-oxidizing environment, otherwise, Fe_3O_4 might also be oxidized. This would critically affect the physical and chemical properties of the magnetic nanoparticles. The precipitated

powder was then isolated by applying an external magnetic field, and the supernatant was removed from the precipitate by decantation. The powder was washed and the solution was decanted twice after centrifugation at 4500 rpm for 15 min. Then 0.01 M HCl was added to neutralize the anionic charge on the particle surface. The cationic colloidal particles were separated by centrifugation and peptized by watering. The obtained magnetic mud was then redispersed in a 200 mL portion of trisodium citrate solution (0.5 M) and heated at 90 °C for 40 min under magnetic stirring at 750 rpm. An appropriate amount of acetone was added to remove the excessive citrate groups adsorbed on the nanoparticles and collected with a magnet. After coating, the product was washed to remove the physically adsorbed surfactant on the particle. The powder was freeze-dried at -60 °C.

1.6. Embedment of Fe_3O_4 nanoparticles in $mSiO_2$ matrix

A solution of ethanol, water, NaOH, sodium citrate and 50 mL of the solutions of previously synthesized MSNs were prepared in two separate containers. The whole solution was consisted of 395 mL ethanol, 36 mL water, 0.24 g NaOH and 0.11 g sodium citrate. 1.5 g of synthesized MNPs were added to the containers and centrifuged three times at 4000 rpm, each for 15 min. The solution was subsequently washed with deionized water. The resulting powders were initially dried in the oven for 12 h at 50 °C and was further heated for 6 h at 560 °C, which resulted in the final drying of powder through calcinations process. The decomposition of EG at this stage provided the required porosities to incorporate MNPs into the pores of the silica matrix. Small amount of carbon in the pores of silica which is the consequence of template removal is essential for the bonding between Fe_3O_4 and SiO_2 .

1.7. Synthesis of colloidal gold nanoparticles (AuNPs)

In a 1 L round-bottom flask equipped with a condenser, 500 mL of 1mM $HAuCl_4$ was brought to a boil with vigorous stirring. Rapid addition of 50 mL of 38.8 mM sodium citrate to the vortex of the solution resulted in a colour change from pale yellow to burgundy. After boiling the solution for 10 min, the heating mantle was removed and stirring was continued for an additional 15 min.

1.8. Coating $m\text{SiO}_2\text{-Fe}_3\text{O}_4$ nanocomposite with Au shell

Gold nanoparticles were coated on the magnetic/silica nanocomposites surfaces in a two-stage process:

(1) Dative binding between amino groups of the surface and gold:

0.32 g of $m\text{SiO}_2\text{-Fe}_3\text{O}_4$ nanocomposites were added to 110 mL of ethanol. 5 mL of colloidal gold nanoparticles were then added to 1 mL of the above solution and incubated at 4 °C overnight. This makes strong dative bonds between the empty orbital of Au and electrons of amino group on the nanocomposites. On the other hand, the binding between gold and the magnetic molecules are of electrostatic type. Therefore, at this stage, gold molecules are bonded to the surface by both dative binding and attractive electrostatic interactions.

(2) Reduction of gold shell on nanocomposites:

The resultant solution from the previous stage was centrifuged twice at 4000 rpm and after it has been washed and rinsed for three times, the obtained powder was dispersed in 4 mL of deionized water. 1.5 mL of HAuCl_4 (1 wt.%) was added to the solution and stirred for 30 min. Then, 200 mL of deionized water and 100 mL of formaldehyde as a reducing agent were added to the solution to form a complete layer of Au around $m\text{SiO}_2\text{-Fe}_3\text{O}_4$. Several cycle of centrifuging and rinsing with deionized water was done to remove un-reacted agents. The change in colour was observed after 3 min. Gold nanoshells were washed three times, centrifuged at 4000 rpm and the final powder was obtained after freeze-drying at -60 °C. Figure 1 represents the schematic illustration of synthesized Au coated $m\text{SiO}_2\text{-Fe}_3\text{O}_4$ nanocomposite.

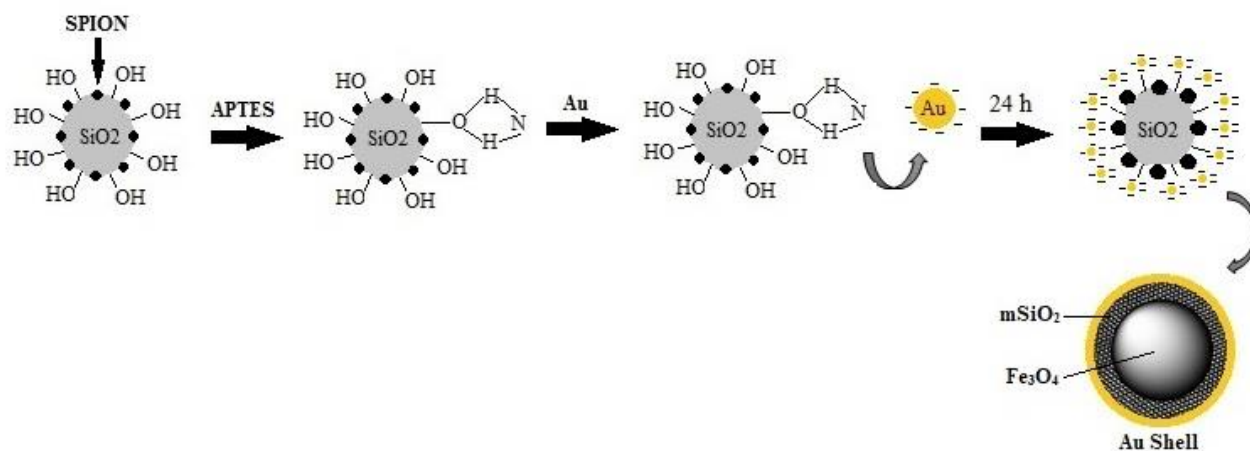


Figure 1. Synthesis procedure of Au-coated magnetic / mesoporous silica nanocomposites

2. Results and Discussion

2.1. NH_2 functionalized silica nanoparticles

The shape and size of nanoparticles were studied using SEM (Figure 2 a) and TEM (Figure 2 b) and as it seen, the silica nanoparticles are spherical with an average diameter of about 70 nm. It is noteworthy that the addition of amino groups helps to avoid the aggregation of nanoparticles. AFM is another

alternative for studying the nanoparticles and the variations on the surface irregularities such as morphology and surface texture. Figures 2c and 2d represent 1-D and 3-D AFM images of SiO_2 respectively prior to porosity. Recently, we have demonstrated that an AFM-based interferometric technique can be used to measure a gold nanoshell thickness with an enhanced accuracy and temporal resolution [33].

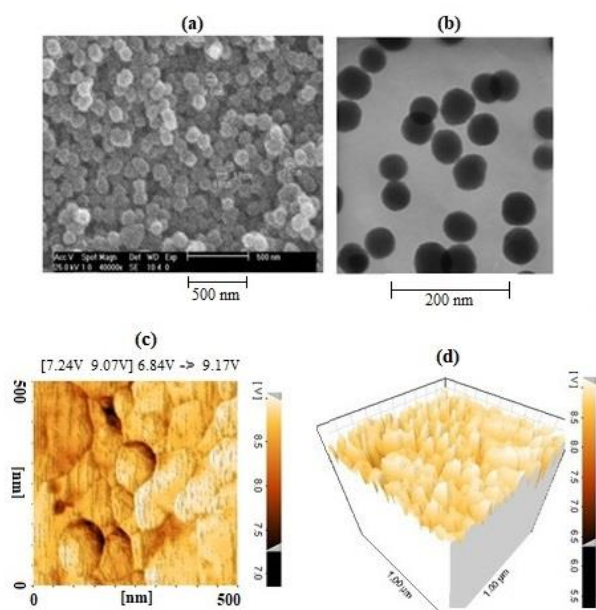


Figure 2. a SEM, b TEM micrographs, c 2-D and d 3-D AFM images of silica nanoparticles

Infrared spectroscopy offers a wealth of information regarding the structure of the surface of the nanoparticles. In particular, IR spectroscopy affords insight into the order and packing of the surface chains. The surface of the core particles is often modified with bi-functional molecules to enhance coverage of shell material on their surfaces. The surface of core particles e.g. silica can be modified using bi-functional organic molecules such as APTMS. This molecule has a methoxy group at one end, and NH group at the other end. APTMS forms a covalent bond with silica particles through the OH group and their surface becomes NH-terminated. Figure 3a shows FTIR spectra of functionalized silica with amine groups (APTES) in the wavenumber range of 400 to 4000 cm^{-1} . The FTIR peak at around 466 cm^{-1} shows Si-O-Si bending mode and that at in the range of 750-850 cm^{-1} corresponds to NH_2 . The peak at 1087 cm^{-1} is associated with Si-O-Si vibration modes. Primary amines ($-NH_2$), secondary amines ($-NH$) and tertiary amines (without hydrogen) show peaks in different wavenumbers. The primary amines show two peaks, one with a broader peak at 3335 cm^{-1} and one minor peak around 1650 cm^{-1} associated with NH_2 asymmetric stretch. The NH and NH_2 peaks indicate the functionalization of silica surface with

amine groups. Figure 3b indicates the chemical microanalysis technique of the synthesized nanoparticles using EDAX where a homogenous distribution of silica nanoparticles can be observed.

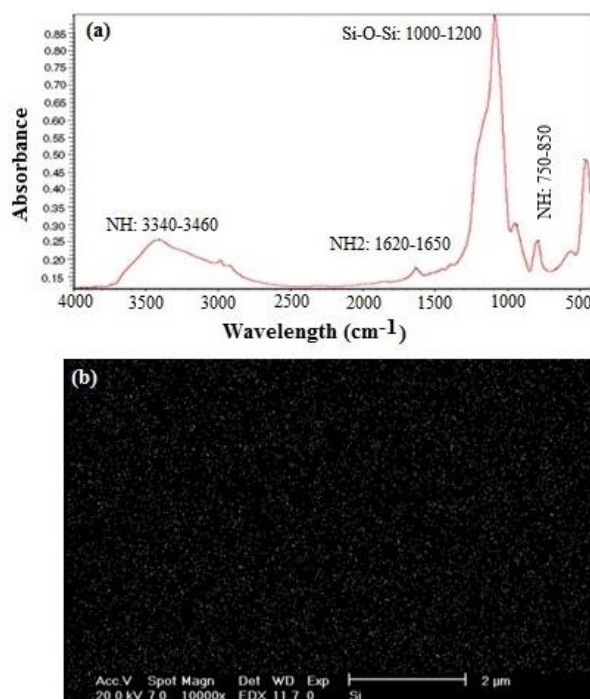


Figure 3. FTIR spectra of functionalized silica with APTES amine groups a and b EDAX image of homogenous distribution of silica nanoparticles

2.2. Analysis of mesoporous silica ($mSiO_2$)

The FTIR analysis of $mSiO_2$ nanoparticles fabricated using different ratios of TEOS to EG is given in Figure 4a for 0.1 and 4b for 0.6 respectively. The wavenumbers associated with primary amines and silica that were previously shown in Figure 3 are also seen here. A relatively sharp peak was observed for Si-C at 970.95 cm^{-1} . The presence of this peak can further confirm the bonding of silicon and active carbons due to the calcinations of $mSiO_2$. It was expected to observe sharper peaks for Si-C for the $mSiO_2$ nanoparticles made with higher contents of EG (higher porosity) due to larger amounts of carbon. However, the obtained results presumably indicate that the molar ratio of EG in these samples (with the weight ratio of 0.6) is larger than the optimum amount.

Mohammad KHOSROSHAHI, Iman TEHRANI, Alireza NOURI

Fabrication and characterization of multilayer $mSiO_2@Fe_3O_4@Au$ mesoporous nanocomposite

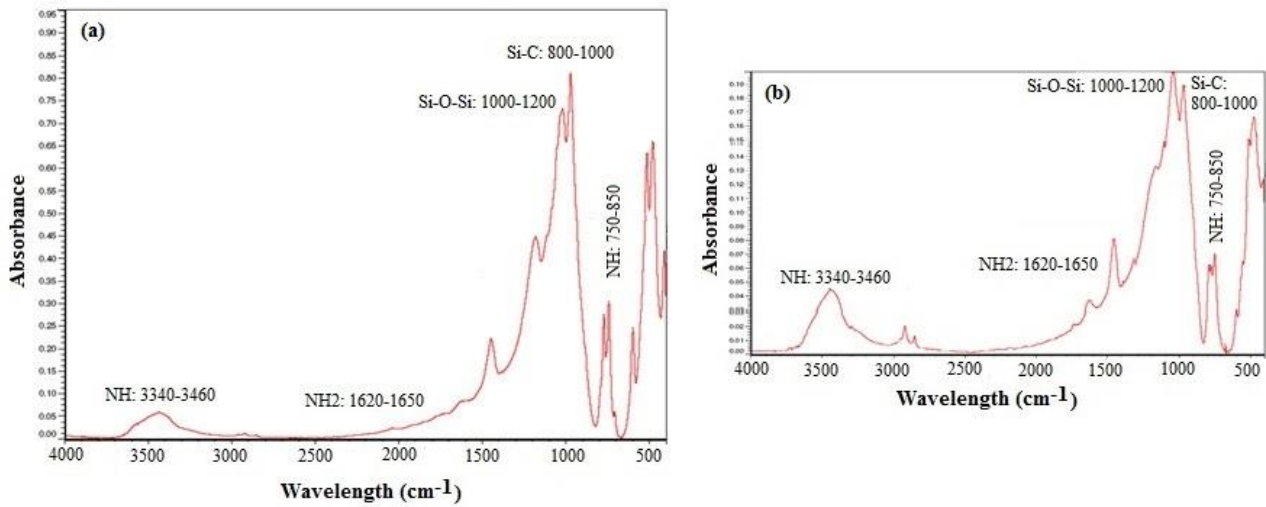


Figure 4. FTIR spectra of mesoporous silica nanoparticles synthesized with a the EG/TEOS molar ratio of 0.1 with 30% porosity and b with 0.6 ratio and 60% porosity

The SEM analysis of $mSiO_2$ nanoparticles are shown in Figure 5. The SEM micrographs of the samples with EG /TEOS molar ratio of 0.1 and the porosity of 30% are shown in different magnifications in Figs 5 (a, b). Figures 5 (c, d) show the sample with EG/TEOS molar ratio of 0.6 with porosity of 60%. The

formation of $mSiO_2$ matrix through the sintering process is clearly seen. Apparently in spite of what was reported by Jain et al. [34], increasing the volume ratio of EG does not necessarily lead to an increase in porosity and it appears that there to be an optimum point.

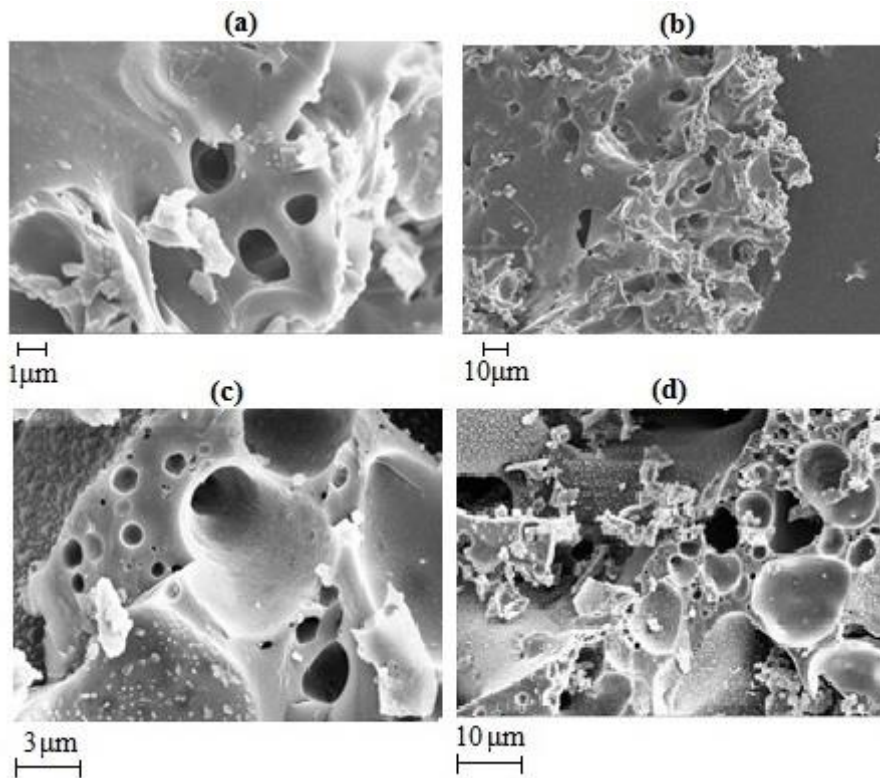


Figure 5. SEM micrographs of the samples with EG /TEOS molar ratio of a, b 0.1 and the porosity of 30% and c, d with molar ratio of 0.6 with porosity of 60%

The surface areas were calculated with BET method [35] using isotherm adsorption data at P/P_0 from 0.05 to 0.30; where P_0 is the saturated vapor pressure of liquid nitrogen at 77 K. The pore volume and pore size distributions were obtained from an adsorption branch by using the BJH method [36]. These methods were conducted at standard pressure at 300 °C using BEL (Japan, Inc). At this temperature,

the gas and air that were entrapped inside the pores would leave and allow the nitrogen to fill up the pores. As shown in Figure 6a, the average radius of pores calculated by BJH method is approximately 15.5 nm. The range of porosity is from 10 to 100 nm, with the major distribution of pore size of less than 20 nm. The BJH analysis shows the pore size distribution peak on 12.2 nm, as seen in Figure 6a.

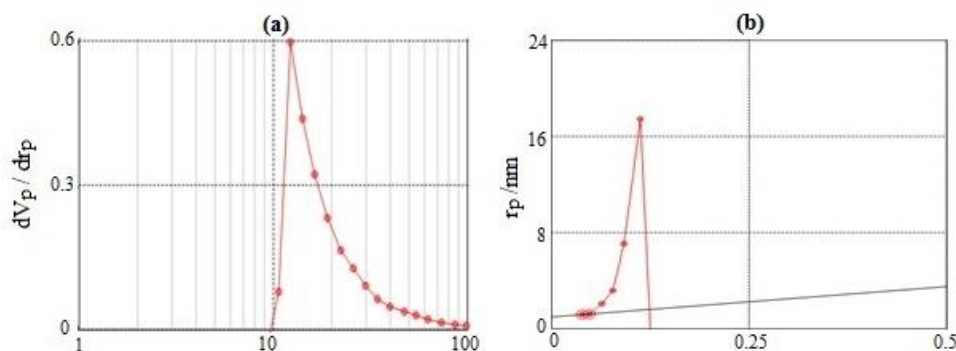


Figure 6. a The BJH analysis of sample pores with an average pores radius size of 15.5 nm and a distribution peak about 12.2 nm and b the S_{BET} of 0.712 m^2/g calculated for sample made with EG/TEOS molar ratio of 0.1

Porosity (ϵ) is defined as a ratio of the pore volume (V_p) to the total volume of the material (V_T), which is the total volume of pores and the volume of material (V_m), $\epsilon = V_p/V_m$.

$$\epsilon = V_p / V_T = V_p / (V_p + V_m) \quad (1)$$

$$V_m = M / \rho_m \quad (2)$$

In the present study the pore volume (V_p) was found 0.0526 cm^3/g . V_m was calculated by dividing 1 g of the material (M) to the density of silica ($\rho_{SiO_2} = 2.2 g/cm^3$). Given the above equations, value of porosity for 1 g of material is 10.3%. The difference between this value with the value of porosity reported by Jain et al. [34] is due to the difference in synthesis of MSNs in these two studies. In the present study, after the decomposition of EG molecules in the oven at 560 °C, some pores are closed as a result of sintering and the attachment of silica nanoparticles, hence preventing the adsorption of nitrogen in the pores. However, by embedding the MNPs before calcinations process, they can be readily placed in the pores. The size of MNPs should be smaller than the $mSiO_2$ matrix. It is notable that the samples made with the 0.6 volume ratio of EG to TEOS did not respond to the BET method due to the closure of pores or the operator errors. The surface area due to its role in equilibrium

adsorption capacity in porous materials is a crucial parameter. Using BET equation, estimation can be made for surface area of a sample:

$$\frac{X}{V_a(1-X)} = \frac{1}{V_M Y} + \frac{(Y-1)X}{V_M Y} \quad (3)$$

where $X = p/p_0$, V_a is the volume of adsorbed gas, and V_M is the molar volume of adsorbed gas on the first layer and Y is the ratio of time of adsorbed molecules to the time of adsorbed molecules on the next layers. Within the distance of 0.25-0.5X by

drawing the values of $\frac{X}{V_a(1-X)}$ as a function of X ,

a straight line can be drawn where V_M can be calculated via the slope of the line and y-intercept ($X=0$). The area of BET for a porous sample can be calculated by the following equation:

$$S_{BET} = 4.371 V_M \quad (4)$$

For the sample made with volume percentage of 0.1 EG to TEOS, S_{BET} was calculated 0.712 m^2/g from the slope of the line shown in Figure 7b.

2.3. Fe_3O_4 nanoparticles

The Figure 7 indicates the SEM (Figure 7a) and TEM (Figure 7b) of synthesized MNPs. Some degree

of agglomeration and overlapping can be seen as darker regions in TEM. The attractive dipole interaction can be argued as follow. Many molecules are partially polar and have a net electric dipole moment, $\mu_d = Ql$. Here, $Q = q_1q_2$ is the electric charge and l is the scalar distance. The vector electric field \vec{E} produced by an electric dipole μ_d can be written

$$\vec{E} = C' \left[\frac{\mu_d}{r^3} - \frac{3(\mu_d \cdot r)}{r^5} r \right] \quad (5)$$

This polar field resembles the magnetic field B of a bar magnet, where C' is the coulomb constant $k = (4\pi\epsilon_0)^{-1}$, the overall strength of the dipole field is $\frac{C'\mu_d}{r^3}$ and r is the distance from dipole center to the field point. A second dipole μ_{d2} will attract this field as $U = -\mu_{d2} \cdot \vec{E}$. Thus, the interaction energy U is about [37]

$$U \cong -\frac{C'\mu_{d1}\mu_{d2}}{r^3} \cong -\frac{C' \ell_0^2 e^2}{r^3} \quad (6)$$

Taking a value $\mu_d = e \ell_0$, the force associated with this interaction is $-\frac{dU}{dr}$, this dipole-dipole force is attractive and the strength is

$$F \cong -\frac{3C'_2\mu_{d1}\mu_{d2}}{r^4} \quad (7)$$

Thus, the above arguments show that at early times where the NPs are likely more dispersed in the base medium will be displaced faster and freely and when they gradually become agglomerated they become less mobile with lower degree of freedom. The variation of the number of NPs with respect to time due to agglomeration is

$$-dN_p/dT = k_g N^n \quad (8)$$

where k_g is the agglomeration rate coefficient and n is the reaction order. As seen in Figure 7c, the particle size distribution analysis showed a particle diameter range between (28-50) nm with a narrow peak distribution at about 34 nm.

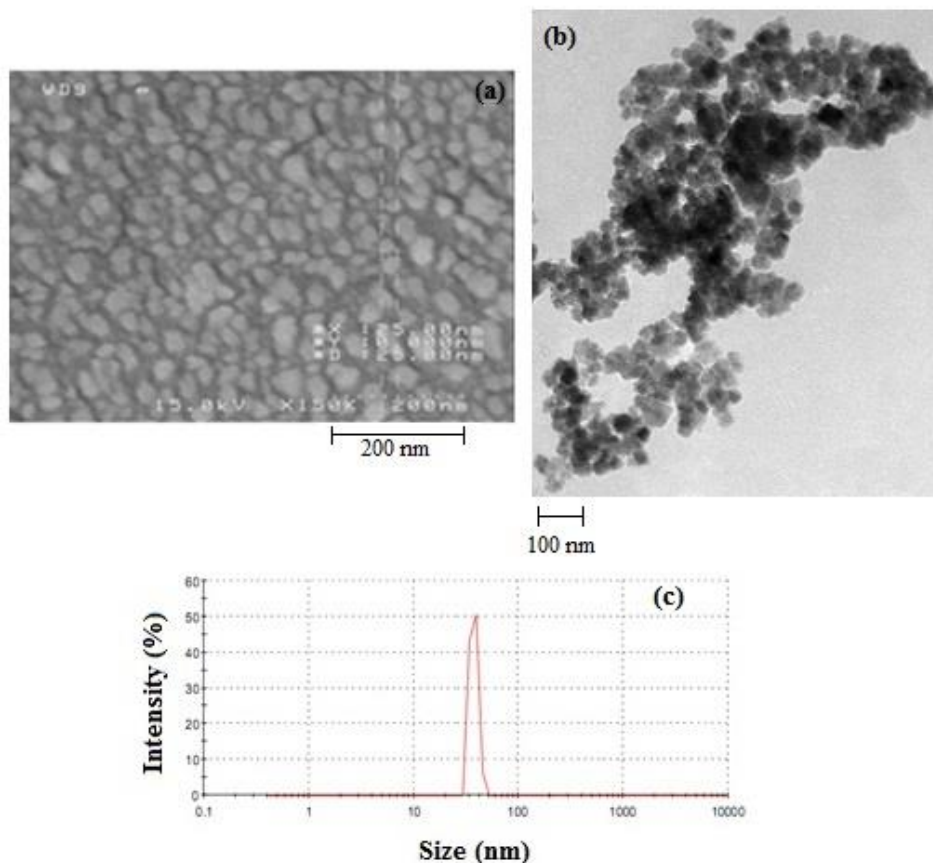


Figure 7. a SEM b TEM micrographs of synthesized MNPs and c the particle size distribution of MNPs with a narrow peak distribution at about 34 nm

Figure 8a shows the XRD result of crystalline structure of MNPs where it confirms the formation of highly purified magnetite phase of iron oxide with diffraction peaks at (111), (220), (311), (400), (422), (511), (440), (533), which are the characteristic peaks of the Fe_3O_4 inverse spinel structure (JCPDS file No. 19-0629) without any interference with other phases of Fe_xO_y . The FTIR result in Figure 8b indicates the two main absorptions centered around 591 and 3422 cm^{-1} , which correspond to Fe-O and H-O-H stretching

mode of vibration of the free or adsorbed water respectively. The absorption peaks around 1614 and 1391 cm^{-1} seen in Figure 8c corresponds to citrate-treated Fe_3O_4 NPs which are characteristics of the carboxylate (COO-Fe) bond. It reveals that trisodium citrate has been successfully grafted onto the surface of Fe_3O_4 NPs through the reaction of hydroxide radical groups on the surface of Fe_3O_4 with carboxylate anion of trisodium citrate.

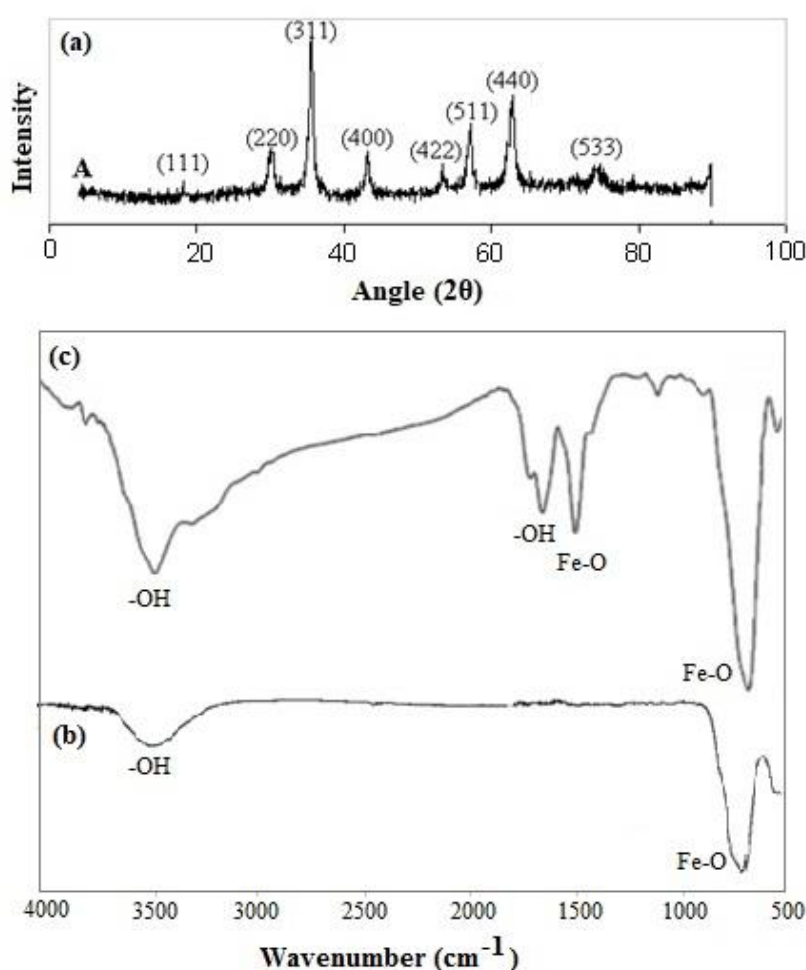


Figure 8. a XRD of crystalline structure of MNPs, b the FTIR spectra of MNPs with two main absorptions corresponding to Fe-O and H-O-H stretching mode of vibration and c the absorption peaks corresponding to citrate-treated Fe_3O_4 NPs with carboxylate (COO-Fe) bond characteristics

2.4. $m\text{SiO}_2/Fe_3O_4$ nanocomposites

The corresponding SEM micrographs of distribution of MNPs at different magnifications embedded within the $m\text{SiO}_2$ matrix made with the EG/TEOS volume ratio of 0.1 and 0.6 are seen in Figures 9 (a, b) and Figures 9 (c, d) respectively. By

comparison, it is evident that there is more homogenous distribution of MNPs within the $m\text{SiO}_2$ matrix made with the EG/TEOS volume ratio of 0.1. The calcination process for the samples with the EG/TEOS volume ratio of 0.6 resulted in agglomeration of silica nanoparticles together and the distribution of areas with no or less porosities.

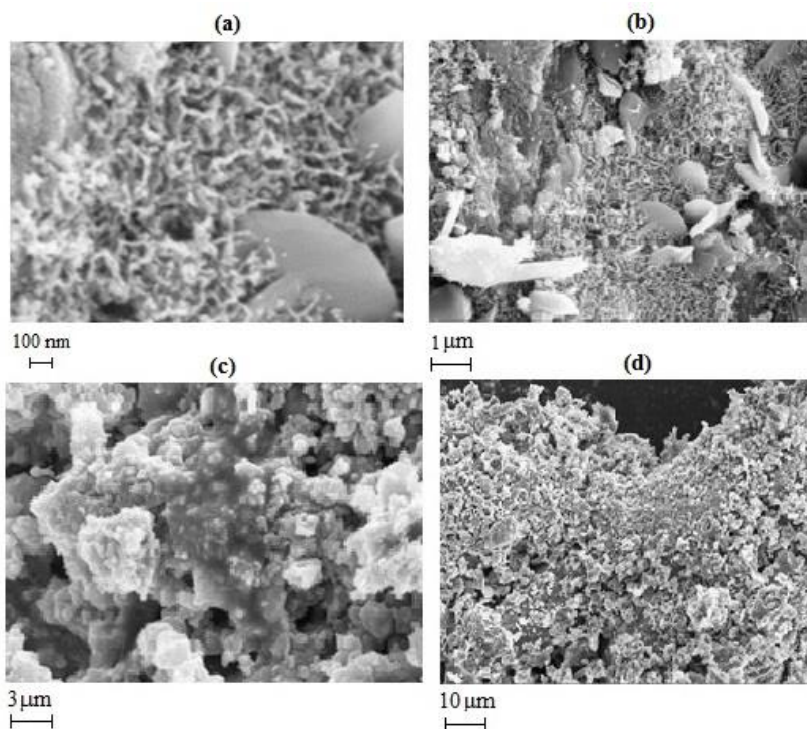


Figure 9. SEM micrographs of MNPs embedded within $mSiO_2$ matrix prepared with the EG /TEOS volume ratio of a, b 0.1 and c, d 0.6 shown at different magnifications

Figure 10a shows the XRD analysis of magnetic/mesoporous silica nanocomposites made with the EG /TEOS volume ratio of 0.1. Given the amorphous nature of silica, its presence in the structure does not lead to any new peak as compared to the XRD results of MNPs shown in Figure 8a. The peaks observed for the angle of $2\theta < 30^\circ$ are associated with the formation of sodium silicate crystals due the bonding of silica and sodium citrate

on the surface of magnetic nanoparticles. The magnetic hysteresis curve of $mSiO_2 / Fe_3O_4$ nanocomposites with EG /TEOS volume ratio of 0.1 is shown in Figure 10b where the value of saturation magnetization reaches to about 6.5 emu/g. The reduced value of nanocomposite magnetization has already been reported by Zhang et al. [38], where it is attributed to the presence of nonmagnetic contents of silica and surface capping molecules.

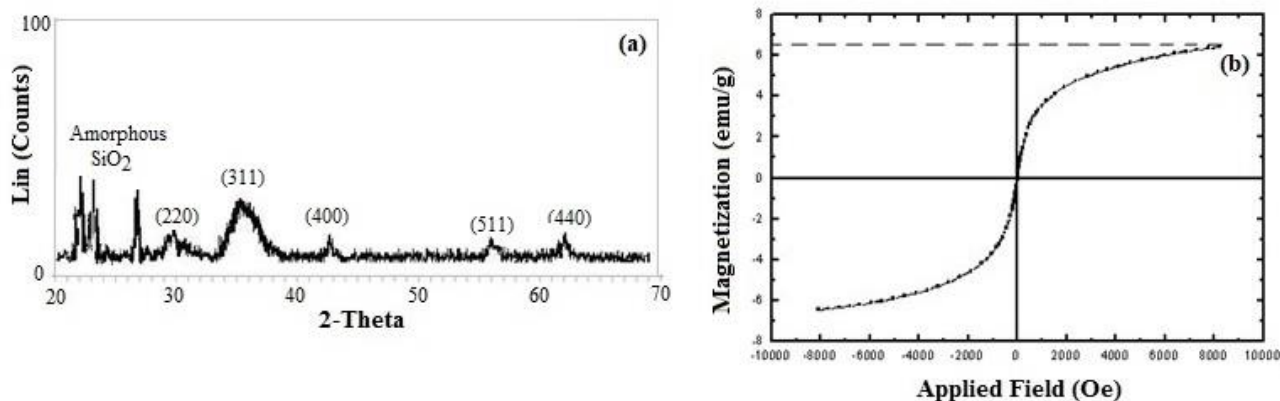


Figure 10. a XRD analysis and b magnetic hysteresis curve (VSM) of magnetic $mSiO_2$ nanocomposites made with EG /TEOS volume ratio of 0.1

2.5. Characterization of AuNPs

Figure 11a shows the XRD of AuNP colloids where three characteristic peaks can be identified as $2\theta = 38.20^\circ$, 44.41° , and 64.54° corresponding to (111), (200) and (220) reflection planes (No. 04-0784) of the Au fcc-cubic phase, indicating that the gold

particles are crystallized. The UV-Vis absorption spectroscopy of Au colloids shown in Figure 11b indicates the dominant peak at 550 nm indicating the formation of AuNPs. An example of AFM image of AuNPs with an approximate average size of 25 nm is displayed in Figure 11c.

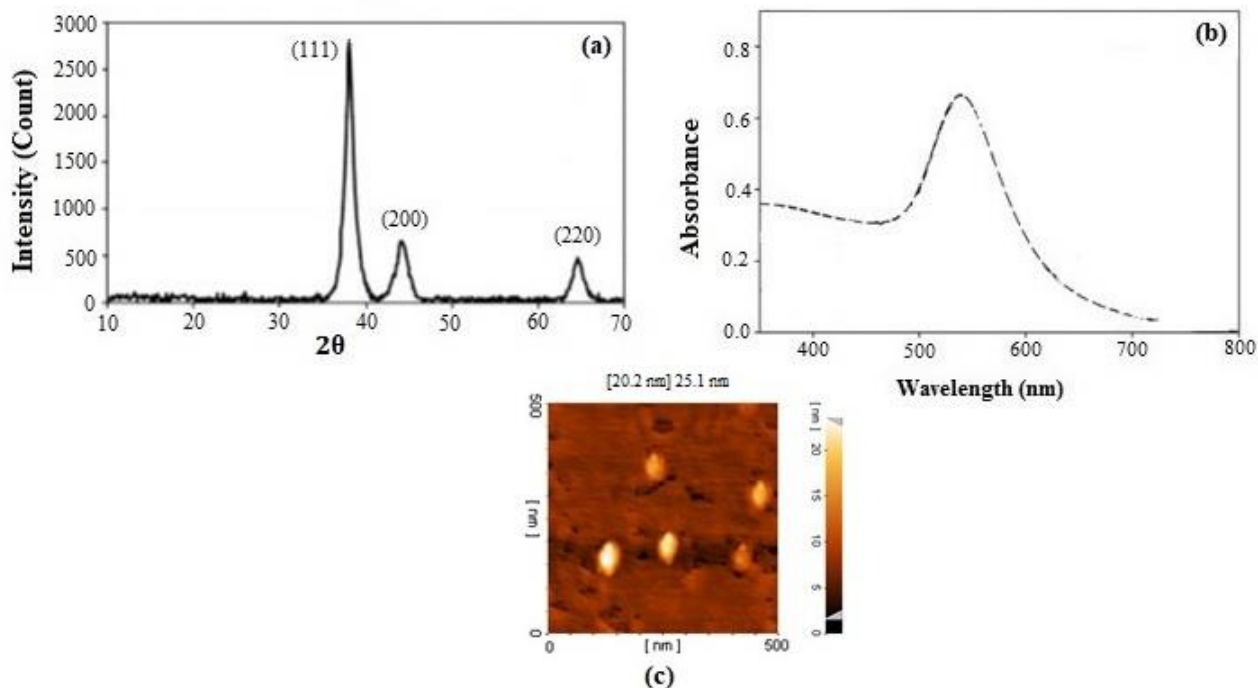


Figure 11. a XRD, b UV-Vis absorption spectroscopy of Au colloids and c an example of AFM image of AuNPs with an approximate average size of 25 nm

2.6. Characterization of Au-coated $mSiO_2 / Fe_3O_4$ nanocomposites

Figure 12a shows a nm narrow particle size distribution between (130-200) with a peak around 157 nm. Figure 12b show 1-D AFM image of nanocomposites synthesized by the procedure described earlier in the material and methods section. The corresponding 3-D image of the surface morphology indicating its roughness variation is shown in Figure 12c. These images provide useful information about surface topography and the size of nanocomposites with well-defined clarity, which effectively is correlated to optical absorption spectra. The gold layer can stabilize the MNPs by sheltering the magnetic dipole interaction. Meanwhile, upon the increase of the particle size, their shape become more regular and spherical. Also, amine-functionalized silica NPs (treated with APTS) is expected to exhibit heavy coverage of gold NPs.

An AFM microscope has the capacity to be used in different operating modes in such a way that one can study the roughness or morphology of surface in different scales. In the application of this approach the displacements of the surface points from the reference plane are modeled as a random surface and characterized by appropriate distribution of the height function (roughness) values z . The peak-to-valley roughness describes the maximum observed range in a sample area and is given by the distance between the highest peak (Z_{max}) and the lowest valley (Z_{min}) on the measured surface, where (Z) indicates the vertical height of the surface. The average roughness (R_{avg}) is the mean value of the surface height (Z) relative the centre plane, which is determined by equating the volumes enclosed by the image of the surface above and below the plane and given by the equation:

Mohammad KHOSROSHAHI, Iman TEHRANI, Alireza NOURI

Fabrication and characterization of multilayer mSiO₂@Fe₃O₄@Au mesoporous nanocomposite

$$R_{avg} = Z_{max} - Z_{min} \quad (9)$$

$$R_{avg} = \sum_{n=1}^N \frac{|Z_n - \bar{Z}|}{N} \quad (10)$$

where (N) is the number of point in the sample area. In our case, $R_{avg} \approx 13$ nm calculated by SPM software.

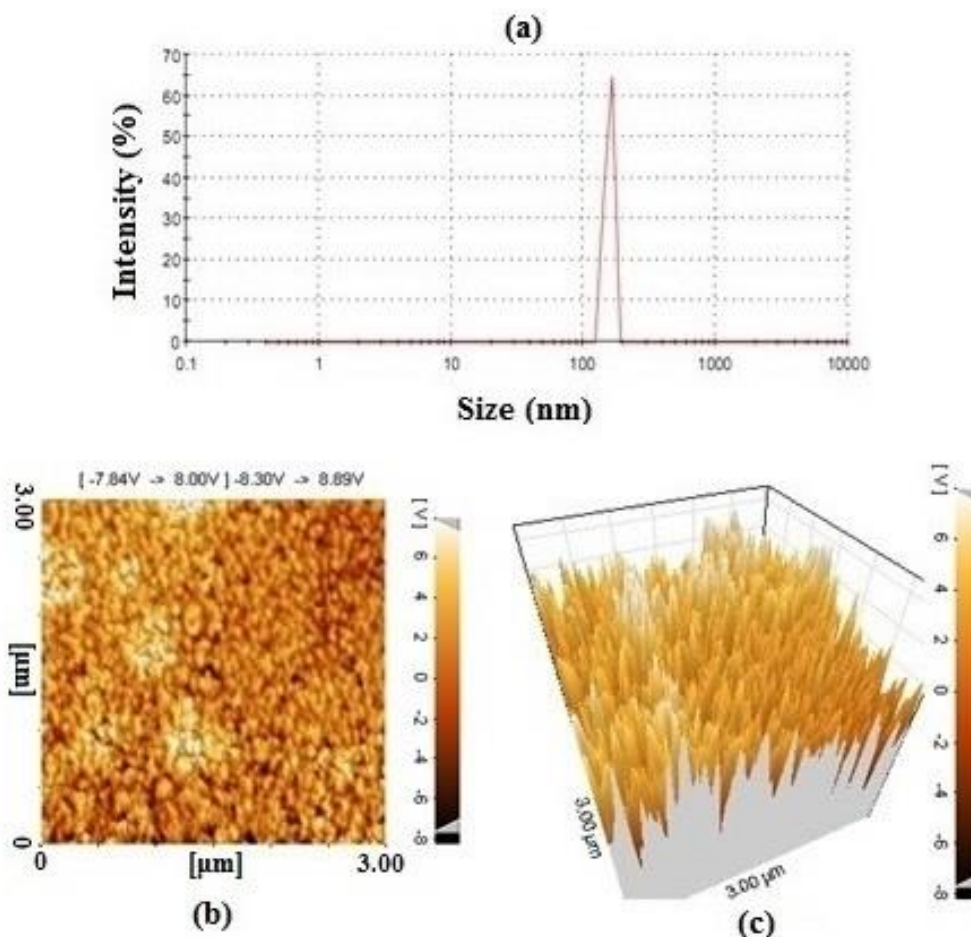


Figure 12. a Particle size distribution of Au-coated mSiO₂/ Fe₃O₄ nanocomposites with a peak around 157 nm, b 2-D and c 3-D AFM image of the nanocomposites

The UV-Vis optical absorption spectrum of Au-coated mSiO₂/Fe₃O₄ nanocomposite is given in Fig.13a. The optical absorption spectrum range of nanocomposite is relatively broad compared with that of pure gold colloid. According to Mie's theory [39], the broadening of resonance absorption is related to the size, shape, and aggregation of the AuNPs. The intensity of UV-Vis spectra has increased compared to pure AuNPs shown in Figure 11b mainly due to shell thickness. Increase in shell thickness is expected to cause a corresponding increase in extinction coefficient due to a larger amount of plasmonic metal per particle. When gold particles aggregate on the surface of amino-modified

silica, the peak surface plasmon resonance wavelength (λ_{SPR}) will shift to the near-infrared range. As it is seen in Figure 13a, λ_{SPR} of obtained nanocomposite is red-shift close to 800 nm, which coincides with highest penetration depth of NIR-IR laser through tissue in therapeutic window. Furthermore, the silica layer provides a dielectric interface for red-shifting the plasma resonance in electromagnetic spectrum resulting from the charge variation of the AuNPs within the core/shell structure. It is known that the core composition and a different core radius/shell thickness ratio of the nanocomposites can influence the SPR wavelength of the Au nanoshell [40-44].

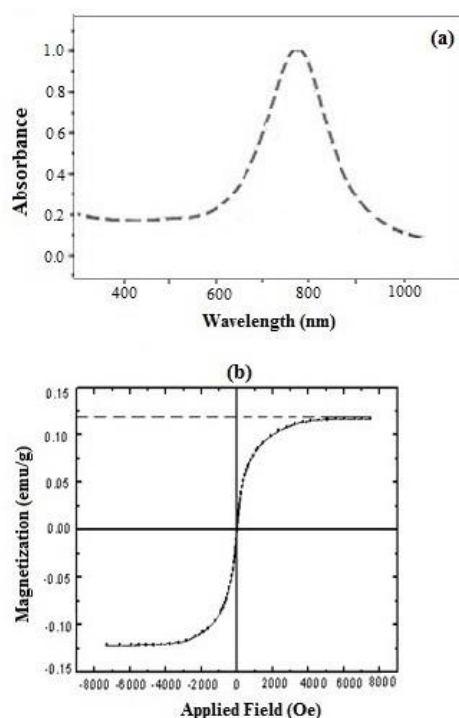


Figure 13. a UV-Vis absorption spectrum and b magnetic hysteresis curve (VSM) of the Au-coated $mSiO_2/Fe_3O_4$ nanocomposite prepared with EG / TEOS volume ratio of 0.1

The extent of the red-shift by self-assembly or aggregation of nanoparticles depends on the number of nanoparticles in ensemble as well as the distance between them. In a larger assembly each particle would be subject to the near-field of a large number of particles, resulting in a much stronger coupling and hence a larger red-shift. The magnetization as a function of applied magnetic field of the Au-coated $mSiO_2/Fe_3O_4$ nanocomposite at 300 K prepared with EG / TEOS volume ratio of 0.1 is seen in Figure 13b. Clearly, the presence of gold shell on magnetic

nanoparticles reduces the magnetization of $mSiO_2/Fe_3O_4$ nanocomposite i.e., from 6.5 emu g^{-1} to about 0.12 emu g^{-1} in Figure 10b. No hysteresis loop is observed in either cases, which implies their superparamagnetic behaviour.

Conclusion

In the present study, a three-layered nanocomposite of magnetic-mesoporous silica-gold ($mSiO_2@Fe_3O_4@Au$) was synthesized using ethylene glycol template and its structural, magnetic and optical properties were characterized. Two types of mesoporous silica were prepared using different volume ratio of 0.1 and 0.6 ethylene glycol to TEOS. The larger volume ratio of ethylene glycol did not result in higher level of porosity in the mesoporous silica structure. Both the width and the intensity of UV-Vis spectrum of Au-coated $mSiO_2/Fe_3O_4$ nanocomposite were higher than pure AuNP. The $\lambda_{SPR} \approx 550 \text{ nm}$ of AuNPs was red-shift close to 800 nm for Au-coated $mSiO_2/Fe_3O_4$ nanocomposite. Hysteresis curves exhibited a superparamagnetic property for $mSiO_2/Fe_3O_4$ and Au-coated $mSiO_2/Fe_3O_4$ nanocomposites but with a lower magnetization in the latter case. Considering the biocompatibility of all used nanomaterials, we believe the suggested nanocomposite can be utilized for drug delivery, magnetic delivery of cargo and PTT by taking advantage of pores size and NIR SPR where available solid state OPO lasers can easily operate within the therapeutic window for biomedical applications.

Acknowledgements

The project is supported by AUT faculty research grant program.

References

- [1] Corot C, Robert Ph, Idée J, Port M, Recent advances in iron oxide nanocrystal technology for medical imaging. *Adv Drug Deliv Rev.* 2006; 58:1471-1504;
- [2] Liu Z, Liu Y, Yao K, Ding Z, Tao J, Wang X, Synthesis and magnetic properties of Fe_3O_4 nanoparticles. *J Mater Syn Proc.* 2002; 10: 83-7;
- [3] Chertok B, David A, Moffat B, Yang V, Substantiating in vivo magnetic brain tumor targeting of cationic iron oxide nanocarriers via adsorptive surface masking *Biomaterials.* 2009; 30: 6780-7;
- [4] Khosroshahi M E, Ghazanfari L, Physicochemical characterization of $Fe_3O_4/SiO_2/Au$ multilayer nanostructure. *Mat Chem Phys.* 2012; 133: 55-62;

- [5] Kuznetsov A, Application of magnetic liposomes for magnetically guided transport of muscle relaxants and anti-cancer photodynamic drugs. *J Mag Mag. Mat.* 2001; 25:95-100;
- [6] Khosroshahi M E, Ghazanfari L, Hassannejad Z, Lenhert S, In-vitro application of doxorubicin loaded magnetoplasmonic thermosensitive liposomes for laser hyperthermia and chemotherapy of breast cancer. *J Nanomed Nanotechnol.* 2015; 6: 298-303;
- [7] Yang P, Gai S, J. Lin J, Functionalized mesoporous silica materials for controlled drug delivery. *Chem Soc Rev.* 2012;41: 3679-98;
- [8] Jin Y, Li A, Hazelton SG, Liang S, John CL, et al., Amorphous silica nanohybrids: Synthesis, Properties and applications. *Chem Rev.* 2009; 253: 2998-3014;
- [9] Ansari L, Malaekheh-Nikouei B, Magnetic silica nanocomposites for magnetic hyperthermia applications. *Int J Hyper.* 2017;33: 354-63;
- [10] He Q, Shi J, Chen F, Zhu M, Zhang L, An anticancer drug delivery system based on surfactant-templated mesoporous silica nanoparticles. *Biomaterials.* 2010; 31: 3335-44;
- [11] Lai C, Trewyn B, Kenftinija K, Xu S, A Mesoporous silica nanosphere-based carrier system with chemically removable CdS nanoparticle caps for stimuli-responsive controlled release of neurotransmitters and drug molecules. *J Am Chem Soc.* 2003; 125: 4451-559;
- [12] Cai W, Hofmeister H, Riner T, Chen W, Optical properties of Ag and Au nanoparticles within the pores of monolithic mesoporous silica. *J Nanopart Res.* 2001; 3: 443-53;
- [13] Wang Y, Gu H, Core-shell type magnetic mesoporous silica nanocomposites for bioimaging and therapeutic agent delivery. *Adv Mat.* 2014; 27: 576-85;
- [14] Wu P, Zhu J, Xu Z, Template-assisted synthesis of mesoporous magnetic nanocomposite particles. *Adv Func Mater.* 2004;14: 345-351;
- [15] Mehmood A, Ghafar H, Yaqoob S, Gohar U, Mesoporous silica nanoparticles: a review. *J Develop Drugs.* 2017;6: 1000174;
- [16] Lu A, Li W, Kiefer A, Schmidt W, Fabrication of magnetically separable mesostructured silica with an open pore system. *J Am Chem.Soc.* 2004; 126: 8616-7;
- [17] Pang J, Luan Y, Yang X, Jiang Y, Functionalized mesoporous silica particles for application in drug delivery system. *Mini Rev Med Chem.* 2012; 12: 775-88;
- [18] Croissant J, Qi C, Maynadier M, Cattoen X, Raehm L, Multifunctional gold-mesoporous silica nanocomposites for enhanced two-photon imaging and therapy of cancer cells. *frontiers Mol Biosci.* 2016; 3: 1-9;
- [19] Yu X, Zhu Y (2016) Preparation of magnetic mesoporous silica nanoparticles as a multifunctional platform for potential drug delivery and hyperthermia. *Sci Tech Adv Mater.* 20156; 17: 229-38;
- [20] Shawky S, Abo-ElHassan A, H. Lilli, Bald H, Efficient loading and encapsulation of anti-tuberculosis drugs using multifunctional mesoporous silicate nanoparticles. *J Nanosci Curr Res.* 2016; 1: 1000103;
- [21] Liberman A, Mendez A, Trogler W, Kummel A, Synthesis and surface functionalization of silica nanoparticles for nanomedicine. *Surf Sci Rep.* 2014; 69: 132-58;
- [22] Ma, Chen H, Chen, Wang X, Au capped magnetic core/mesoporous silica shell nanoparticles for combined photothermo-/chemo-therapy and multimodal imaging. *Biomaterials.* 2012; 33: 989-98;
- [23] Liu Y, Xu M, Chen Q, Guan G, Gold nanorods/mesoporous silica-based nanocomposite as theranostic agents for targeting near-infrared imaging and photothermal therapy induced with laser. *Int J Nanomedicine.* 2015; 10: 4741-61;
- [24] Lu F, Popa A, Zhou S, Zhou J, Iron oxide-loaded hollow mesoporous silica nanocapsules for controlled drug release and hyperthermia. *Chem Commun.* 2013; 49: 11436 - 8;
- [25] Shao D, Lu M, Zhao Y, Zhang F. The shape effect of magnetic mesoporous silica nanoparticles on endocytosis, biocompatibility and biodistribution. *Acta Biomaterialia.* 2017; 49: 531 - 40;

- [26] Zhao W, Gu J, Zhang L, Chen H, Fabrication of uniform magnetic nanocomposite spheres with a magnetic core/mesoporous silica shell structure. *J Am Chem Soc.* 2005; 127: 8916-7;
- [27] Silva S, avallaie R, Sandiford L, Tilley R, Gold coated magnetic nanoparticles: from preparation to surface modification for analytical and biomedical applications. *Chem Commun.* 2016; 52: 7528-40;
- [28] Oldenburg S, Jackson J, Westcott S, Halas N, Infrared extinction properties of gold nanoshells. *J Appl Phys Lett.* 1999; 75: 2897 - 900;
- [29] Huang X, El-Sayed I, Qian, W, El-Sayed M. Cancer cell imaging and photothermal therapy in the near-infrared region by using gold nanorods. *J Am Chem Soc.* 2006;128: 2115;
- [30] Khosroshahi ME, Mandelis A, Lashkari B, Frequency-domain photothermoacoustic ultrasonic imaging of blood and opto-thermal effects of plasmonic nanoparticle concentrations. *J Biomed Opt.* 2015; 20: 076009;
- [31] Khosroshahi ME, Ghazanfari L, Hassannejad Z, Effect of laser wavelengths on drug release with and without gold nanoshells and magnetic guidance on uptake by cancer cells. *J Nanomed Res.* 2017; 6: 1-10;
- [32] Khosroshahi M E, Tajabadi M, Multifunctional nanoplatform for targeted laser-induced hyperthermia and microscopy of breast cancer cells using SPION-based gold and folic acid conjugated nanodendrimers: An in vitro assay. *J Nanomed Nanotech.* 2017; 8: 432-43;
- [33] Khosroshahi M E, Ghazanfari L, Dual mode atomic force microscopy and interferometric scattering imaging of single $Fe_3O_4@Au$ nanoshell synthesized for biomedical applications. *Nano Res. Appl.* 2017; 3: 1-8;
- [34] Jain A, Rogojevic S, Ponoth S, Agarwal N, Porous silica materials as low-k dielectrics for electronic and optical interconnects. *Thin Solid Films.* 2001; 398: 513-22;
- [35] Brunauer S, Emmett P, Teller E, Adsorption of gases in multimolecular layers. *Am Chem Soc.* 1938; 60: 309-19;
- [36] Barrett E, Joyner L, Halenda P, The determination of pore volume and area distributions in porous substances. *J Am Chem Soc.* 1951; 73: 373-80;
- [37] Khosroshahi M E, Ghazanfari L, Preparation and characterization of silica-coated iron-oxide bionanoparticles under N_2 gas. *Physica E.* 2010; 42: 1824-9;
- [38] Zhang Y, Gong S, Jin L, Li S, Magnetic nanocomposites of Fe_3O_4/SiO_2 -FITC with pH-dependent fluorescence emission. *Chinese Chem Lett.* 2009; 20: 969-72;
- [39] Scholz S M, Vacassy R, Dutta J, Hofmann H, Mie scattering effects from monodispersed ZnS nanospheres. *J Appl Phys.* 1998; 83: 7860-4;
- [40] Wang Y, Shen Y, Xie A, Li S, A Simple Method To Construct Bifunctional Fe_3O_4/Au Hybrid Nanostructures and Tune Their Optical Properties in the Near-Infrared Region. *J Phys Chem C.* 2010; 114: 4297-301;
- [41] Oldenburg S, Averitt R, Westcott S, Halas N, Nanoengineering of optical resonances. *J Chem Phys Lett.* 1998; 288: 243-7;
- [42] Jain P, Lee K, El-Sayed I, El-Sayed M, Calculated absorption and scattering properties of gold nanoparticles of different size, shape, and composition: applications in biological imaging and biomedicine. *J Phys Chem B.* 2006; 110: 7238-48;
- [43] Khosroshahi M E, Hassannejad Z, Synthesis and evaluation of time dependent optical properties of plasmonic magnetic nanoparticles. *Opt Mat.* 2013; 32: 644-51;
- [44] Khosroshahi M E, Ghazanfari L, Simulation and experimental results of optical and thermal modeling of gold nanoshells *Mat Sci Eng C.* 2014; 42: 185-91.